

High-speed confocal fluorescence imaging with a novel line scanning microscope

Ralf Wolleschensky

Bernhard Zimmermann

Carl Zeiss MicroImaging GmbH
Carl-Zeiss-Promenade 10
07745 Jena
Germany

Michael Kempe

Carl Zeiss AG
Carl-Zeiss-Promenade 10
07745 Jena
Germany

Abstract. Research in the life sciences increasingly involves the investigation of fast dynamic processes at the cellular and subcellular level. It requires tools to image complex systems with high temporal resolution in three-dimensional space. For this task, we introduce the concept of a fast fluorescence line scanner providing image acquisition speeds in excess of 100 frames per second at 512×512 pixels. Because the system preserves the capability for optical sectioning of confocal systems, it allows us to observe processes with three-dimensional resolution. We describe the principle of operation, the optical characteristics of the microscope, and cover several applications in particular from the field of cell and developmental biology. A commercial system based on the line scanning concept has been realized by Carl Zeiss (LSM 5 LIVE). © 2006 Society of Photo-Optical Instrumentation Engineers. [DOI: 10.1117/1.2402110]

Keywords: confocal; scanning microscopy; fast dynamics; fluorescence imaging; depth discrimination.

Paper 05371RR received Dec. 8, 2005; revised manuscript received Aug. 18, 2006; accepted for publication Aug. 21, 2006; published online Dec. 26, 2006.

1 Introduction

Today's basic biomedical research centers around investigations of complex dynamic processes in cells, tissues, and model organisms. These processes take place at different timescales and within different spatial ranges (see Fig. 1 for four major experimental areas). In particular, these research activities encompass questions regarding the ontogenesis of organs and organisms and investigations of signal transmission pathways mediated by ions within cells and through membranes, as well as vesicle and protein transport processes within cells. In today's postgenomic world, all the above-mentioned questions are tightly related to the more general question of how identified proteins are networked in cells and cell tissues. Ultimately, understanding of those dynamic networks is key for the development of innovative pharmaceutical treatment techniques. Furthermore, once developed, such new techniques must be evaluated using live cell imaging approaches. Within the framework of these questions, living cells, organs, and whole organisms in the intact state need to be analyzed and manipulated accordingly.

Confocal laser scanning microscopes play a pivotal role in addressing these questions because they enable the highly resolved visualization of biological material. Up to now, however, "high resolution," referred largely to spatial resolution, while the temporal resolution of these instruments often remained clearly behind the speed of many biological processes. To answer such questions, a suitable microscope system would need to fulfill the following requirements. First, to image subcellular structures and cellular domains, it must provide optical resolution on the order of or better than several

100 nm. This resolution needs to be maintained even in whole organisms like zebra fish or mouse embryos. Second, to fulfill the requirements of a significant set of applications, the acquisition frame rate has to be in the range of tens to hundreds of frames per second, so that dynamic processes taking place at timescales down to milliseconds can be visualized in an xyt image (boxes 1 to 3 in Fig. 1). In addition, microscope systems are required that are able to record processes, such as mitotic events or aspects of embryonic development (box 4 in Fig. 1). While the latter often proceed at considerably slower speeds, they often take place within extended volumes. They, therefore, are required to capture snapshots of complete three-dimensional (3D) scenes within seconds or less, again asking for XY -image acquisition rates of 100 frames per second or more. Both speed and optical resolution requirements should not compromise the detection sensitivity. This would enable the study of light sensitive and weakly stained samples, whereby imaging is not influencing the function of the sample. In summary, Fig. 1 demonstrates that ideal microscope systems need to be flexible to image at different optical resolutions and different acquisition rates. Moreover, in several biological applications when imaging cellular or multicellular structures, the optical resolution can be traded for sensitivity and acquisition rate.

Several approaches have been taken to achieve fast confocal imaging. The concepts can be categorized into fast single point scanning systems and systems where the sample is illuminated and signals are detected in parallel.¹ Commercial fast point scanning systems use acousto-optical beam deflectors (Noran Odyssey) or resonance scanners (Nikon RCM-8000). Given the fundamental limits set by the emission of fluorescence photons from typical stained specimens, a microscope

Address all correspondence to R. Wolleschensky, Carl Zeiss MicroImaging GmbH, Carl-Zeiss-Promenade 10, 07745 Jena, Germany; Tel: +49/364164-3677; Fax: +49/36412847272; E-mail: Wolleschensky@zeiss.de

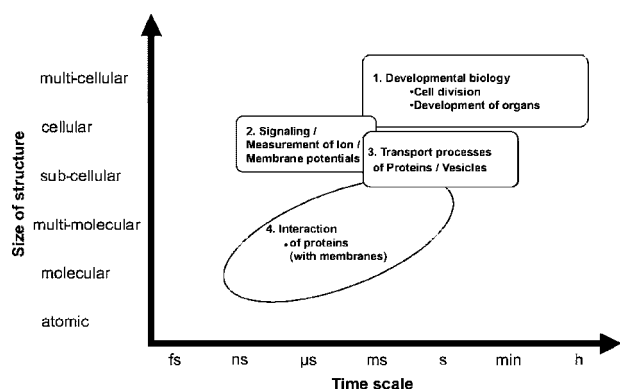


Fig. 1 Major experimental areas: monitoring fast dynamics and kinetics or dynamic 3D structures without causing detrimental effects by observation.

should preferably exhibit some parallelization in the excitation and detection process. Otherwise the intensity needs to be very high to acquire a sufficient fluorescent signal during the short pixel dwell time. One concept for systems with parallel acquisition uses multiple spots that raster scan over the sample, which we call multipoint laser scanning microscope. In the literature, this has been also referred to as Nipkow-type spinning disk microscopes (Yokogawa). Another approach is to illuminate and detect complete lines rather than points of the image that we call line scanning laser microscope (L2M). Galvanometer scanners are used to scan the line across the sample. The capability for 3D imaging is ensured by detecting the fluorescence light excited along the line with a slit-shaped line detector. Such a configuration has been introduced by Brakenhoff et al.² and Corle et al.³ L2M systems have been commercially marketed in the Meridian Insight and the Bio-Rad DVC 250 microscopes. However, both systems had limited sensitivity due to the conventional dichroics that separate the fluorescence light from the excitation light and the rescanning of the fluorescence light after the slit aperture onto matrix sensors. Because of the used detection scheme, dark noise is an important factor, since the sensor is not only measuring in the areas where the sample is illuminated, but in the complete scan field. Here we will discuss in detail a novel concept of the L2M. This system uses an entirely new concept to achromatically separate the fluorescence from the excitation light. A fast line sensor that can be read out in parallel allows for a flexible adaptation of the frame sampling, which is needed to match the frame sampling to the optical resolution. In case of weak fluorescence signals, the frame sampling (pixel size) can be traded for sensitivity or frame speed.

For a point scanning microscope with finite-sized slit and point detectors, a description of the optical transfer function (OTF) has been given by Kawata et al.⁴ A general overview over various concepts of confocal imaging systems with slit apertures can be found in Ref. 5. For the case of two-photon excitation, the line scanning approach was investigated by Guild et al.⁶ In Sec. 2, we give a description of the concept of linewise illumination and detection and compare it with point scanning approaches (single point and point array). A description of the microscope and its experimental evaluation of selected properties is given in Sec. 3. In addition, we present an entirely new solution to separate the light of the sample from

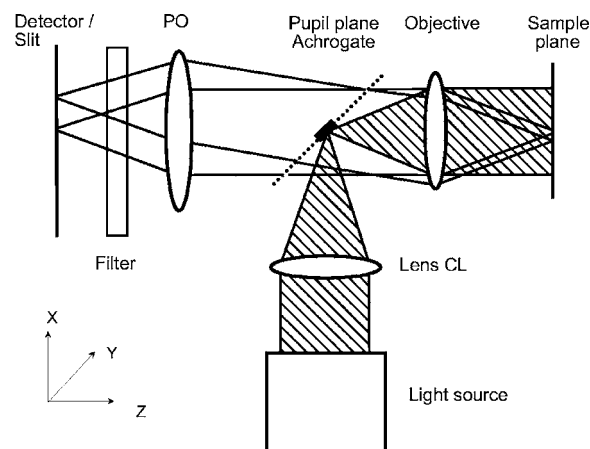


Fig. 2 Schematic setup of the L2M. Collimated light from the light source is focused by a cylindrical lens (CL) onto the beamsplitter that is formed as a narrow reflective stripe (Achromate) sitting in the pupil plane. The objective lens focuses the light in the direction unaffected by CL (not shown) onto the object where fluorescence is excited along a line. The fluorescence is collected by the objective lens, passes the Achromate, and is imaged by the pinhole optics (PO) onto the detector after passing the emission filter. An adjustable slit is situated directly in front of the detector.

excitation light that yields a much improved sensitivity and flexibility. Finally, to highlight the particular features of the microscope, we provide a set of application examples in Sec. 4.

2 Theoretical Considerations

2.1 Basic Equations

In order to discuss the basic imaging performance of the L2M, we use a setup shown schematically in Fig. 2. Using line-forming optics (in the simplest case a cylindrical lens), a line focus is created in the pupil plane in which the beamsplitter for separating the illumination and detection beam paths is situated. Filling the pupil of the objective lens results in a diffraction-limited line illumination in the object plane. The fluorescence generated along this line in the object is imaged via the objective lens and the detector lens onto an adjustable slit in front of a line detector.

For simplicity, we assume the magnification between object plane and camera to be 1. We will restrict our consideration to the case of fluorescence imaging whereby the excitation is produced by spatially coherent illumination. If we assume space invariance of the optical system, the general imaging equation is

$$S(v_x, v_y, u) = PSF(v_x, v_y, u) \otimes O(v_x, v_y, u), \quad (1)$$

where S is the image signal depending on the lateral (v_x and v_y) coordinates and the axial coordinate (u) in the object space, \otimes denotes a convolution of the object function O (density and spatial distribution of the fluorochromes in the object) with the point spread function (PSF)

$$PSF(v_x, v_y, u) = |h_{exc}(v_x, v_y, u)|^2 |h_{det}(v_x, v_y, u)|^2. \quad (2)$$

In Eq. (2), h_{exc} and h_{det} are the excitation and detection amplitude point spread function (APSF), respectively. Throughout this paper, we will use optical coordinates defined as

$$\begin{aligned} v_{x,y} &= \frac{2\pi}{\lambda} \sin \alpha \times (x, y), \\ u &= \frac{8\pi}{\lambda} \sin^2(\alpha/2)z, \end{aligned} \quad (3)$$

where α is the semiaperture angle of the objective lens, λ is the wavelength, (x, y) are the lateral coordinates, and z is the axial coordinate.

The detection PSF depends on the objective lens (APSF: h_{obj}) and the camera [APSF: h_{cam} is the product of the pixel detection sensitivity and the slit opening, see Eq. (9) below]

$$|h_{det}(v_x, v_y, u)|^2 = |h_{obj}(v_x, v_y, u)|^2 \otimes |h_{cam}(v_x, v_y, u)|^2. \quad (4)$$

In order to determine the imaging properties of the L2M, we need to determine the excitation PSF $|h_{exc}|^2$ and the detection PSF $|h_{det}|^2$, respectively. We will start with the excitation PSF. Because the imaging performance of the system is ultimately limited by the objective lens, we can calculate this PSF as the Fourier transform (FT) of the light distribution in the exit pupil of this lens that is produced by the line-forming optics. We assume this distribution to be constant in the y direction and a Gaussian distribution of $1/e^2$ -width w [normalized as the Fourier coordinate k by $\lambda/(2\pi \sin \alpha)$] in the x direction and obtain in paraxial approximation

$$\begin{aligned} h_{exc}(v_x, v_y, u) &= \int_{-1}^1 dk_y \exp(-jk_y v_y) \int_{-1}^1 dk_x \exp(-jk_x v_x) \\ &\quad \times \exp\left\{-\frac{k_x^2}{w^2}\right\} \exp\left\{-j\frac{u}{2}(k_x^2 + k_y^2)\right\}. \end{aligned} \quad (5)$$

Evaluating both integrals separately, assuming that $w \ll 1$ (i.e., the line is much narrower than the pupil), and neglecting irrelevant prefactors, this results in

$$\begin{aligned} h_{exc}(v_x, v_y, u) &= \exp\left\{-\frac{v_x^2}{4(w^{-2} + ju/2)}\right\} \int_{-1}^1 dk_y \\ &\quad \times \exp\left\{-j\frac{u}{2}\left(k_y + \frac{v_y}{u}\right)^2\right\}. \end{aligned} \quad (6)$$

The in-focus excitation PSF ($u=0$) can be calculated from Eq. (6) analytically

$$|h_{exc}(v_x, v_y, 0)| = \exp\left\{-v_x^2 \frac{w^2}{4}\right\} \left(\frac{2 \sin v_y}{v_y}\right). \quad (7)$$

Because $w \ll 1$, in all following considerations, we can neglect the first factor in Eqs. (6) and (7). Practically, this means that we have a constant excitation along the line in the field of view of the objective lens.

Next, we consider the detection PSF neglecting the minor shadowing effect of the Achromate beamsplitter in the pupil plane (which amounts to less than 2% of the energy incident, see Sec. 3.1). According to Eq. (4), it depends on the objective APSF and the camera PSF. The first is given in paraxial approximation as

$$h_{obj}(v, u) = \int_0^1 dk_r J_0(k_r v) \exp\left\{-j\frac{u}{2}k_r^2\right\} k_r, \quad (8)$$

where $v = \sqrt{v_x^2 + v_y^2}$, and k_r is the radial coordinate in the objective pupil. The camera PSF can be written as

$$|h_{cam}(v_x, v_y)|^2 = \begin{cases} 1 & \text{for } (-p \leq v_x \leq p) \text{ and } (-s \leq v_y \leq s) \\ 0 & \text{otherwise} \end{cases}. \quad (9)$$

This means we assume a constant detection sensitivity within a rectangular pixel of width $2p$ that is limited by an adjustable slit of width $2s$ (the extension of the pixel in the y direction is large compared to the slit width). For the following, we make the assumptions that p is much smaller than the extent of the objective PSF on the camera. It can be shown that with this assumption of very small pixels along the line, one obtains nearly the same results as considering more realistically a pixel size according to the Nyquist theorem. Based on this assumption, one obtains from Eqs. (4) and (9)

$$|h_{det}(v_x, v_y, u)|^2 = \int_{-s}^s dv'_y |h_{obj}(v_x, v'_y - v_y, u)|^2, \quad (10)$$

which becomes in the confocal limit ($s \rightarrow 0$)

$$|h_{det}(v_x, v_y, u)|^2 = |h_{obj}(v_x, v_y, u)|^2. \quad (11)$$

The general PSF of the L2M can thus be written using Eq. (2) with Eqs. (6) and (10) as

$$\begin{aligned} PSF(v_x, v_y, u) &= \left| \int_{-1}^1 dk_y \right. \\ &\quad \times \exp\left\{-j\frac{u}{2}\left(k_y + \frac{v_y}{u}\right)^2\right\} \left. \right|^2 \\ &\quad \times \int_{-s}^s dv'_y |h_{obj}(v_x, v'_y - v_y, u)|^2. \end{aligned} \quad (12)$$

As a special case, we give below the confocal in-focus PSF ($u=0, s \rightarrow 0$) that can be obtained analytically

$$PSF_c(v_x, v_y, 0) = \left(\frac{2 \sin v_y}{v_y}\right)^2 \left(\frac{2J_1(\sqrt{v_x^2 + v_y^2})}{\sqrt{v_x^2 + v_y^2}}\right)^2. \quad (13)$$

Equation (13) is formally equivalent to a point scanning laser scanning microscope (LSM) with a slit detector in the confocal limit. It must be emphasized, however, that the general PSF [Eq. (12)] is not the same as the one for such a LSM with finite slit width. This is due to the line illumination.

In all previous considerations, we have neglected the Stokes shift between the illumination and the fluorescence

light. This was to simplify the equations. It can be easily incorporated by introducing a factor $\beta = \lambda_{det}/\lambda_{exc}$ (i.e., the ratio of the fluorescence wavelength detected and the excitation wavelength) and scaling the coordinates of the detection PSF as $\beta v_{x,y}$ and βu , respectively.

The L2M can be used with two-photon excitation of fluorescence. In this case, the fluorescence excited is proportional to $|h_{exc}|^4$ rather than $|h_{exc}|^2$ as in the case of single-photon excitation. Thus the PSF of the L2M with two-photon excitation becomes

$$PSF_{TPE}(v_x, v_y, u) = \left| \int_{-1}^1 dk_y \right. \\ \times \exp \left\{ -j \frac{u/2}{2} \left(k_y + \frac{v_y/2}{u/2} \right)^2 \right\} \Bigg|^4 \\ \times \int_{-s}^s dv'_y |h_{obj}(v_x, v'_y - v_y, u)|^2. \quad (14)$$

Here we have scaled the optical coordinates of the excitation PSF with $\beta=1/2$ to account for the excitation with light of twice the wavelength compared to a corresponding single-photon excitation.

2.2 Depth Discrimination

An important property of laser scanning microscopes is the depth discrimination that allows one to achieve 3D imaging. A good measure for this property is the image of a thin fluorescing layer as a function of axial position. With $O(v_x, v_y, u) = \delta(u)$, one obtains

$$D(u) = \int_{-\infty}^{\infty} \int_{-\infty}^{\infty} dv_x dv_y PSF(v_x, v_y, u). \quad (15)$$

For the limiting cases of confocal ($s \rightarrow 0$) and nonconfocal ($s \rightarrow \infty$), imaging the depth discrimination is given as

$$D_c(u) = \int_{-\infty}^{\infty} \int_{-\infty}^{\infty} dv_x dv_y \left| \int_{-1}^1 dk_y \right. \\ \times \exp \left\{ -j \frac{u}{2} \left(k_y + \frac{v_y}{u} \right)^2 \right\} \Bigg|^2 \\ \times |h_{obj}(v_x, v_y, u)|^2, \quad (16)$$

and

$$D_{nc}(u) = \int_{-\infty}^{\infty} dv_y \left| \int_{-1}^1 dk_y \exp \left\{ -j \frac{u}{2} \left(k_y + \frac{v_y}{u} \right)^2 \right\} \right|^2. \quad (17)$$

In the nonconfocal case, we simply have the integral over the excitation PSF. From the principle of energy conservation, this is independent of u (i.e., there is no depth discrimination) as is to be expected for nonconfocal imaging.

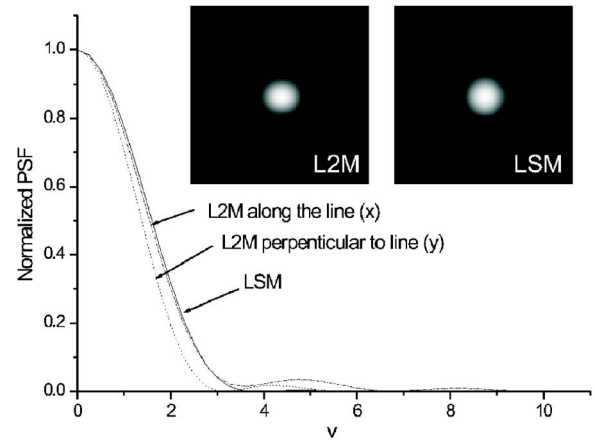


Fig. 3 Calculated normalized lateral PSF of the L2M and the LSM for a detector size of 1 AU. The line lies along the horizontal direction (x). For this detector size, the main peak of the lateral PSF of the LSM is similar to the one of a conventional microscope but exhibits reduced sidelobes that are pronounced in the L2M PSF.

2.3 Comparison of the Imaging Characteristics of Line Scanning and Point Scanning Microscopes

For comparing the imaging characteristics of line scanning with point scanning microscopes as a function of the slit and pinhole size, respectively, we will give the size of the detector either in units of v (called v_d) or in so-called Airy units (AU). This size is the radius in the case of the pinhole (LSM) or the half width of the slit (L2M), respectively. A length scale of 1 AU is defined as $0.61\lambda/\sin \alpha$. Therefore, we have the relation $1 \text{ AU} = 1/(1.22\pi) v_d$ between AUs and the optical coordinate v . Figure 3 shows the lateral PSF for a detector size of 1 AU. It is obvious that the lateral resolution of the L2M is different in the two axes. In the direction along the line (x), the PSF of the L2M is essentially equivalent to the PSF of a nonconfocal LSM (i.e., the Airy function), while in the direction perpendicular to line illumination and detection slit, an intensity distribution similar to a sinc function [see Eq. (13) results for the confocal case]. This distribution is characterized by a somewhat narrower full-width at half maximum (FWHM) compared to the Airy function. The FWHM is shown in Fig. 4, indicating that for a larger detector the mean FWHM of the L2M is somewhat smaller than the one of the LSM. It is to be expected that these minor differences of the lateral PSF do not play a practical role.

A similar comment can be made regarding the differences of the axial distribution that are not shown here. In contrast, the difference in the depth discrimination is a significant one. Figure 5 shows the depth response according to Eq. (13) comparing the LSM and the L2M. An obvious feature is the different falloff of the signal. While the LSM signal falls off with approximately u^{-2} for large u , the L2M signal falls with approximately u^{-1} as is the case for the LSM with slit detector.

Another feature is the faster broadening of the L2M depth response with increased detector size. This can be seen from the FWHM as a function of detector size shown in Fig. 6. In the confocal limit, the FWHM of the L2M is somewhat larger than the FWHM of the LSM. Also, the approximately linear

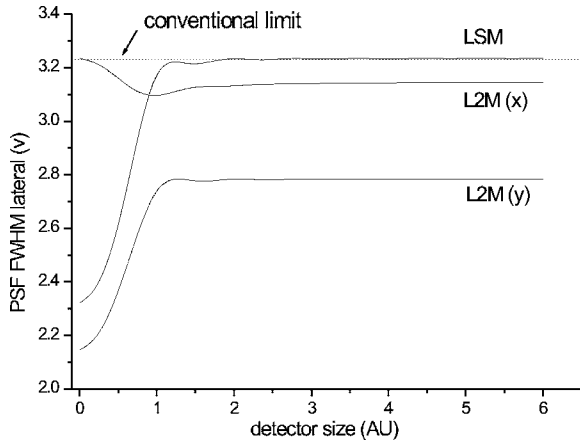


Fig. 4 Lateral FWHM of the PSF as a function of detector size. The FWHM of the L2M PSF behaves similar to the LSM PSF with reduced detector size while along the line the FWHM is nearly independent of the slit width.

increase for larger detector size (>2 AU) has a faster slope in the case of the L2M. The lines in Fig. 6 represent fits based on the following function:

$$FWHM = \sqrt{FWHM_0^2 + (aPH)^2}, \quad (18)$$

where $FWHM_0$ is the FWHM in the confocal limit, and a is a constant of unit (u/AU) representing the slope of the increase. Physically, the two terms below the square root belong to the diffraction limit and the geometrical limit, respectively. The fits yield

$$FWHM_0 = \begin{cases} 8.5 \text{ LSM} \\ 10.8 \text{ L2M} \end{cases} \quad a = \begin{cases} 10.1 \text{ LSM} \\ 15.8 \text{ L2M} \end{cases}. \quad (19)$$

Given the lateral asymmetry of the L2M PSF, one might ask whether the depth discrimination depends on the lateral orientation of object structures. It can be shown that the depth response of the L2M is nearly independent of the orientation

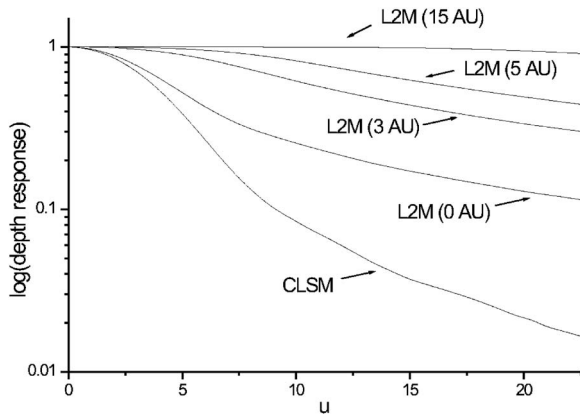


Fig. 5 Depth discrimination of the L2M for different slit sizes in comparison with the LSM in the confocal limit (CLSM). The weaker signal falloff at large distances from focus even in the limit of vanishing slit width is obvious.

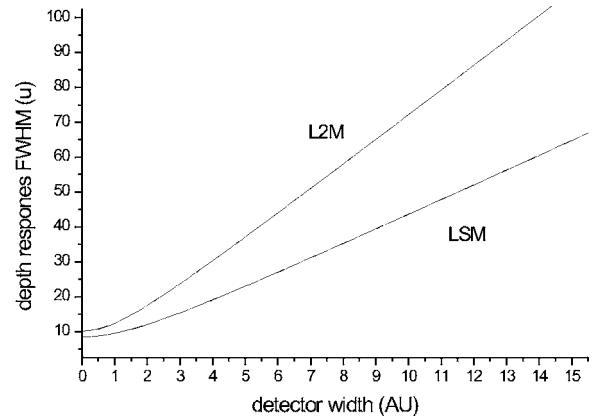


Fig. 6 FWHM of the depth discrimination as a function of detector size for the L2M in comparison to the LSM showing the increasingly broader response of the line scanning system with rising detector size.

of the structures and for line structures inferior to the one of the confocal LSM (CLSM)—as already seen for extended objects (planes).

By imaging deep in thick biological samples, one encounters aberrations, in particular spherical aberrations, induced by the index mismatch between the immersion medium (oil, water) and the biological material.⁷ Such aberrations are known to degrade the image quality. The depth discrimination is particularly sensitive to spherical aberrations. Calculations show that the L2M behaves similar to a point scanning system under such circumstances, that is, it is neither less nor more sensitive to sample induced aberrations than the point scanner.

A different confocal microscope concept for fast imaging uses parallel excitation and detection in multiple discrete spots. Different schemes are currently used to scan the multiple spots across the sample. Nipkow-type microscopes use a spinning disk for scanning, whereas in a different arrangement, galvanometric scanners are applied. Apertures are used to generate the spot patterns. The size of the apertures are often fixed, which is especially the case for spinning disk systems. As will be seen in the next paragraph, depending on the separation of the spots, there is more or less detection cross talk between neighboring pinholes if thick or scattering samples are imaged. This cross talk as well as the sectioning strength depends on the objective lens used [numerical aperture (NA) and magnification], because the diffraction limited spot size (and therefore the size and the separation of the pinholes in AU) varies for a fixed aperture. Because such microscopes also aim at fast fluorescence imaging, it is interesting to compare them with the L2M and the LSM. In the following discussion, such microscopes are referred to as multispot laser scanning microscopes (MSM).

The PSF of the MSM can be deduced similarly to the one of the L2M. However, the excitation APSF needs to be modified by a spatial pattern P , which represents the individual illumination spots. The PSF becomes

$$PSF(v_x, v_y, u) = |h_{exc}(v_x, v_y, u) \otimes P(v_x, v_y)|^2 |h_{det}(v_x, v_y, u)|^2, \quad (20)$$

where h_{exc} and h_{det} are the APSFs of a LSM. For our calculations, we assumed a rectangular pattern of illumination

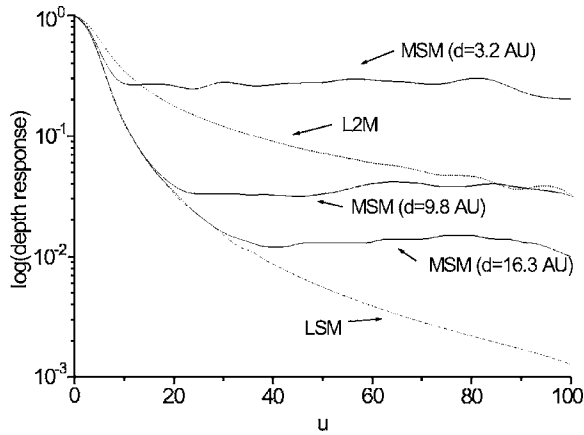


Fig. 7 Depth discrimination of the MSM (pinhole size 1 AU) for different spot distances d in comparison with the LSM and the L2M for the same detector size. The MSM exhibits a large background signal of about one-tenth to one hundredths of the peak signal.

spots with a distance of d , such that P can be calculated by

$$P(v_x, v_y) = \sum_{q=-N}^N \delta(v_x - qd, v_y - qd), \quad (21)$$

where q is a whole number and $2N$ is the number of illumination spots considered. Figure 7 shows the resulting depth discrimination of the MSM for different lateral distances of the illumination spots d . For reference, the LSM and the L2M curves are also shown. All curves have been calculated for detector widths corresponding to 1 AU. It can be seen that for high spatial separations of the illumination spots, the depth discrimination follows the response of the LSM. However, in contrast to the L2M and LSM, a nearly constant background signal is present for large u and gets more pronounced if the distances between the illumination spots are decreased. The strong dependence of the amplitude of the background signal on the distance d suggests that it is coming from the cross talk between adjacent illumination spots that strongly overlap at a certain defocus to generate a nearly widefield-type homogeneous excitation. The influence of the spatial separation of the illumination spots on the FWHM of the depth response is minor as long as the background signal is below half the in-focus amplitude.

The impact of the background signal in the depth response becomes very pronounced in the case of thick fluorescing samples. For the simulations of a thick object, we assume a thick fluorescent dye solution (fluorescent sea) of thickness L (in optical units). Imaging one interface between air and dye gives the so-called edge response of the microscope, which can be calculated from the depth discrimination by

$$R(u) = \int_u^{L+u} D(u') du'. \quad (22)$$

Figure 8 depicts the calculated edge response for the MSM having different spatial separations d between the illumination spots and assuming a layer thickness of $13 \mu\text{m}$ ($\text{NA}=1.4$ and $\lambda=488 \text{ nm}$), which is a typical size of a single cell layer. For reference the curves for the LSM and the L2M are also

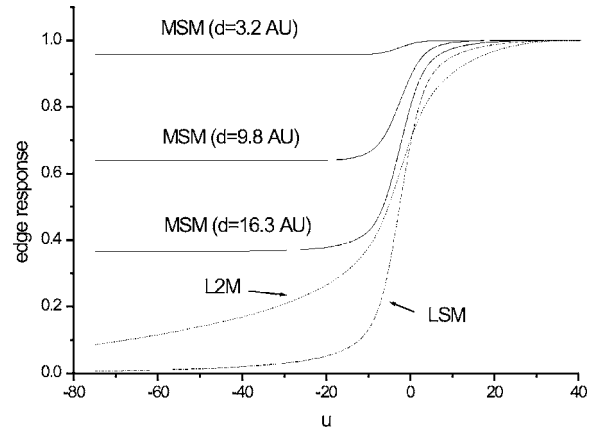


Fig. 8 Edge response of the MSM (pinhole size 1 AU) for different spot distances d in comparison to the LSM and the L2M for a sample thickness of $u=200$ (corresponds to $L=13 \mu\text{m}$ at $\text{NA}=1.4$ and $\lambda=488 \text{ nm}$). All curves have been normalized using the value at $u=40$.

shown. For all curves a detection aperture width corresponding to 1 AU has been considered. In this imaging situation the nearly constant background signal in the depth discrimination of the MSM results in an offset of the edge response outside the sample interface. It is overlaid by a response similar to the one of the LSM at the sample interface. The offset depends strongly on the amount of fluorescent cross talk between adjacent illumination spots, which is determined by the level of the background signal in the depth response and the thickness of the fluorescent layer. The slope at $u=0$ is determined by the FWHM of the depth response. Hence, it is similar for the LSM and the MSM.

This behavior can be modeled assuming that the depth response of the MSM is given as the sum of the depth response of the LSM and a constant background

$$D_{SD}(u) = D_{LSM}(u) + \text{const}(d). \quad (23)$$

If we now calculate the edge response, we get the behavior discussed above

$$R_{SD}(u) = \int_u^{L+u} D_{LSM}(u') du' + \text{const}(d) \times L. \quad (24)$$

In contrast to the other microscopes, the edge response for the MSM is not only influenced by the spatial separation of the illumination spots but also by the sample thickness itself. This has to be taken into account if samples thicker than a couple of cell layers are imaged as will be seen later in this paper. Some discussion on the topic of cross talk in multispot confocal microscopes and further references can be found in Ref. 8.

2.4 OTF

An alternative description of the imaging properties (contrast and resolution) is in terms of the OTF. The OTF is the 3D FT of the PSF [Eq. (12)]. For illustration purposes, we want to consider here two special cases of the confocal systems only: the OTF for thin in-focus objects (lateral OTF) and for a thin fluorescing sheet (axial OTF). The first OTF is given by the

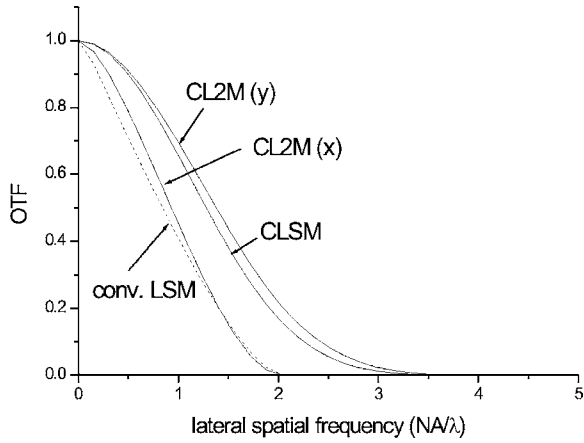


Fig. 9 In-focus OTF in lateral direction for the LSM in the nonconfocal limit (conv. LSM) and in the confocal limit (CLSM) in comparison to the line scanning system with vanishing line width (CL2M). The OTF of the L2M along the line (x) is similar to the one of the convoluted LSM while the OTF perpendicular to the line (y) is nearly identical to the one of the CLSM.

FT of Eq. (13) while the latter is given by the FT of Eq. (15). The lateral OTF shown in Fig. 9 of the confocal L2M (CL2M) in the direction of the line is very similar to the OTF of a nonconfocal LSM (or widefield microscope). Perpendicular to the line, we obtain a result similar to the CLSM. In particular,

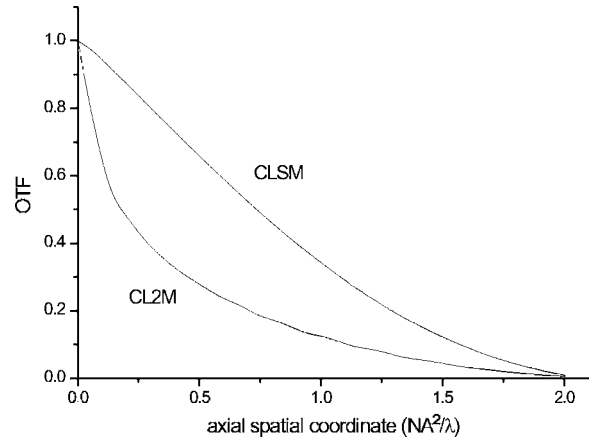


Fig. 10 Axial OTF of the LSM and the L2M in the confocal limit showing the much weaker transfer of spatial frequencies in the case of the L2M.

the frequencies where the OTF becomes zero that mark the fundamental limit of resolution (frequency limits) are identical to the nonconfocal LSM ($l_x=2NA/\lambda$) and the CLSM ($l_y=4NA/\lambda$), respectively. The axial OTF shown in Fig. 10 clearly indicates the weaker sectioning strength of the L2M. However, it is important to note that the frequency limits of the CLSM and the CL2M are identical ($2NA^2/\lambda$). This is the

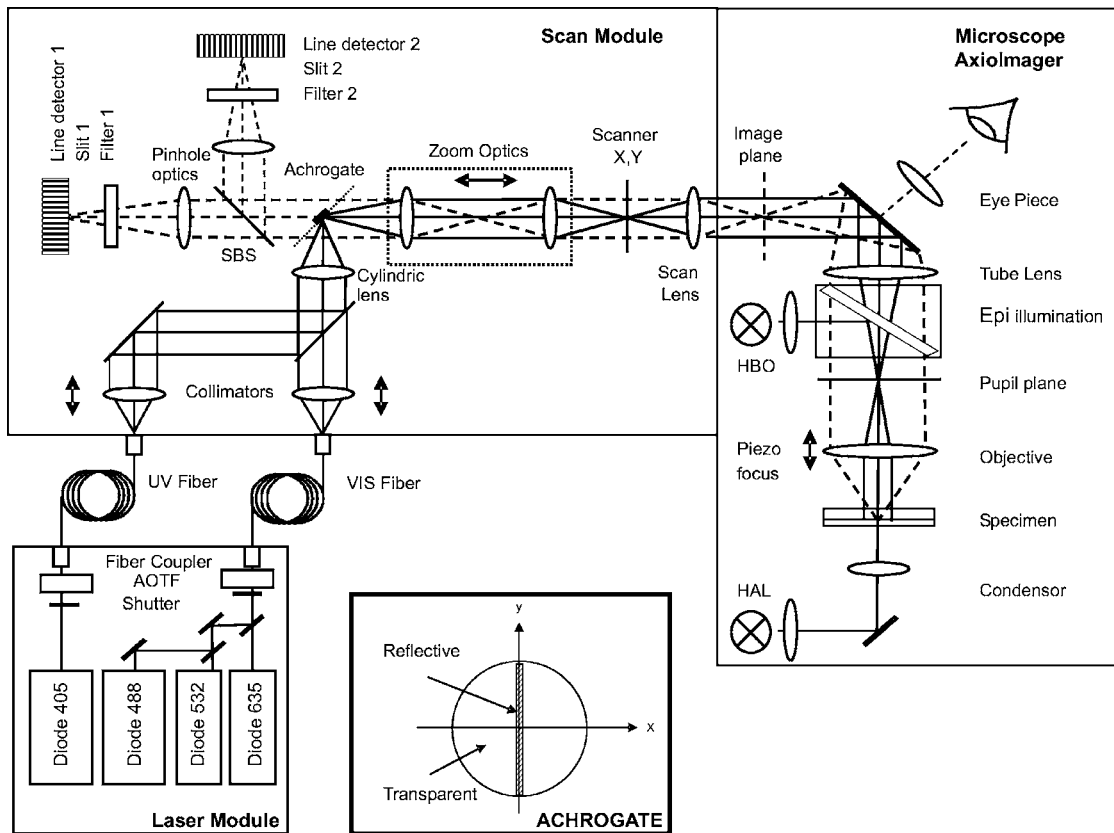


Fig. 11 Schematic of the realized L2M system LSM 5 LIVE. The inset shows a detailed view of the main beamsplitter (Achrogate). AOTF: acousto-optical tunable filter, HBO: mercury lamp for widefield epifluorescence imaging, HAL: halogen lamp for widefield illumination, SBS: secondary beamsplitter for separating the detection channels 1 and 2.

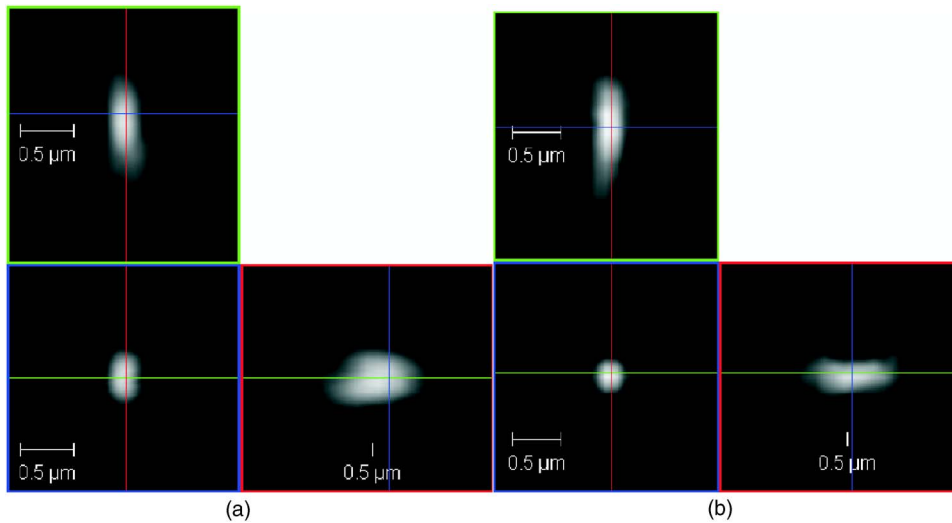


Fig. 12 PSF of the LSM (a) and the L2M (b) in an orthogonal view for a detector size of 1 AU (LSM) and 1.2 AU (L2M), respectively. The objective lens used is a Zeiss Plan-Apochromat 63×/1.4 oil lens imaging 110-nm fluorescing beads. The linear polarization of the incident light is pointing in the vertical direction while the line was oriented in the horizontal direction.

frequency equivalent of the fact that the FWHM of the depth response is very similar in both cases.

From the discussion above, it seems that the imaging performance of the L2M is considerably inferior to the performance of the LSM, since the amplitudes of the transmitted frequencies are lower than the LSM. However, the signal-to-noise ratio on the L2M can be much better compared to a LSM, due to the longer integration times. Depending on the signal strength of the sample, this could result in an overall better transfer of frequencies in the L2M.

3 The Microscope

3.1 The Experimental Setup

Based on the concept of line scanning that has been explained in Sec. 2, Carl Zeiss has designed and built a microscope system termed LSM 5 LIVE. Figure 11 schematically shows this system with a scan module, a laser module, and an upright microscope stand (Axioplan 2i) as the principal components. In order to gain acquisition speed while keeping sufficient sensitivity, the microscope relies on linewise detection of fluorescence signals excited by linewise illumination of the sample as discussed in Sec. 2. To acquire a two-dimensional optical slice, the line focus is scanned across the object plane by using a first galvanometer scanner. The excitation light is

focused to a diffraction-limited line focus by the microscope objective. Fluorescence emitted from the sample was collected by the microscope objective and directed by a dielectric beamsplitter (SBS) to up to two line detectors with 512 pixels, each equipped with barrier filters to block residual excitation light and with adjustable slit apertures for confocal slit detection. The two detectors allow one to simultaneously collect the fluorescence from up to two markers or to detect in addition to one marker the signal produced by a widefield contrast technique using the halogen lamp (HAL), e.g., differential imaging contrast. To collect a 3D image stack, the *z* position of the specimen is varied using either the focus drive of the microscope stand or the piezofocus on the objective lens. Using zoom optics in combination with the two galvanometer scanners, the field of view is adjustable in its size and position relative to the optical axis.

For illumination of the sample, the laser module is equipped with four different lasers producing wavelengths of 405, 488, 532, and 635 nm and connected to the scan module via fibers. It is possible to correct for chromatic aberrations introduced by the objective lens using movable collimation lenses placed behind each fiber, respectively. Acousto-optical tunable filters (AOTFs) are used for fast beam blanking and continuous attenuation of the individual laser lines.

Table 1 Comparison of the FWHM of the PSF in the confocal limit (detector sizes of 0.5 AU–LSM and 0.6 AU–L2M) with vector calculations (Zeiss Plan-Apochromat 63×/1.4 oil, wavelength: 488 nm, β=1.06)

	LSM (μm)			L2M (μm)		
	Lateral (y)	Lateral (x)	Axial	Lateral (y)	Lateral (x)	Axial
Measured ^a	0.15	0.25	0.46	0.18	0.20	0.54
Calculated	0.14	0.18	0.39	0.18	0.23	0.39

^aAfter deconvolution of the measured values ($FWHM_{meas}$) taking into account the bead's diameter ($FWHM_{bead}$) using a Gaussian approximation $FWHM = \sqrt{(FWHM_{meas})^2 - (FWHM_{bead})^2}$.

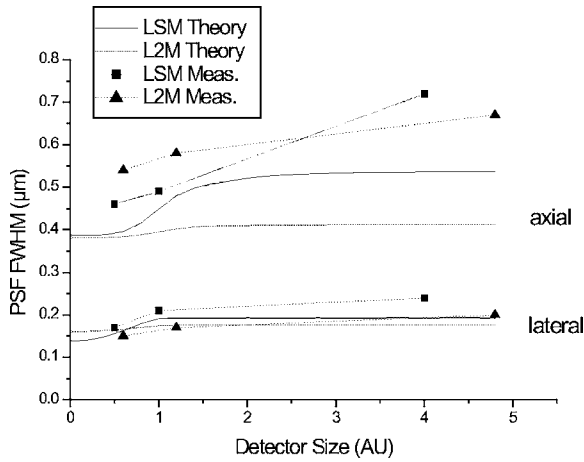


Fig. 13 FWHM of the PSF for the LSM and the L2M. The line connecting the measured points is to guide the eye only. The measured data were deconvolved taking the finite bead size into account as detailed in the caption of Table 1.

Fast imaging relies on very sensitive detection schemes. Apart from the sensor, the optical scheme to separate the fluorescence light from the excitation light is very critical. Conventional chromatic beamsplitters show major drawbacks if a parallel sample illumination and detection is applied, especially when simultaneous illumination with different wavelengths and fast switching between excitation wavelengths are required. For instance, in order to illuminate the whole field of view of 18 mm in the intermediate image plane, the incident angle onto the beamsplitter varies by 20 deg. This reduces the efficiency of the chromatic beamsplitter dramatically, whereby the efficiency becomes dependent upon the position in the field of view.

A new achromatic, angle independent and highly efficient beamsplitter design (Achrogate) is therefore applied to split the excitation light from the fluorescence light. A simplified optical scheme of the microscope is depicted in Fig. 11(b). The microscope uses coherent laser light sources with a collimated Gaussian beam. Anamorphic optics (CL) forms the

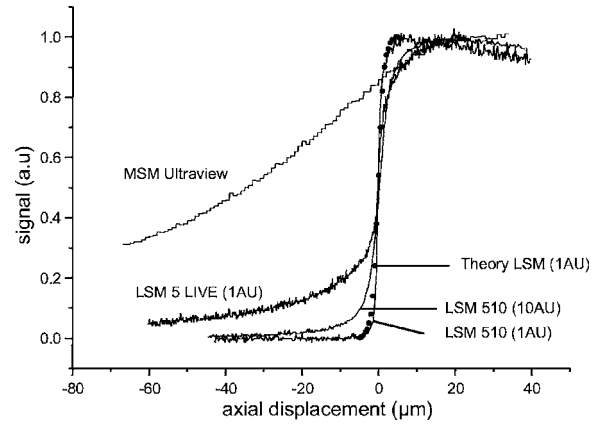


Fig. 14 Fluorescent sea imaging with various microscope systems (Zeiss Plan-Apochromat 63 × /1.4 oil objective lens). For comparison, some calculated spots for the LSM response are shown. All curves were normalized using the largest averaged image value in the z stack.

laser light into a line at the pupil plane of the microscope along the y axis. This results in a line at the sample along the x axis (shaded area in Fig. 2). The line in the pupil is sufficiently long to fill the complete aperture of the pupil ensuring a diffraction limited line in the sample plane.

The generation of fluorescence is an incoherent process, whereby the size of the fluorescent molecules is below the optical resolution of the microscope. Hence, the excited molecules radiate as point sources into all spatial directions. The objective lens collects the fluorescence in such a way that the light is filling the complete back aperture (pupil) of the objective lens (of area A_{pupil}) (lines in Fig. 2). The spatial incoherence of the fluorescence is used to very efficiently separate the illumination and the detection beam paths. For that purpose, the Achrogate beamsplitter is placed in a pupil plane of the microscope. It consists of a reflective area with a line shape (of area A_{RL}) to reflect the illumination beam path. The remaining part of the beamsplitter is highly transparent allowing the fluorescent light to be transmitted toward the detector. The

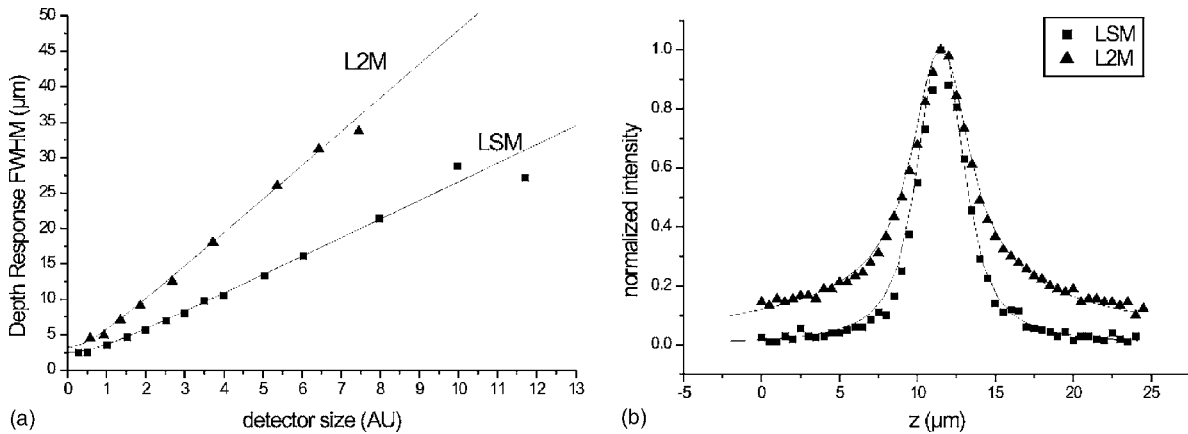


Fig. 15 FWHM of the depth response as a function of detector size (a) and depth response with a 1-AU detector size (b) of the L2M and the LSM for an objective lens Zeiss Plan-Neofluar 20 × /0.5 ($\lambda_{exc}=488$ nm, $\lambda_{fluo}>505$ nm). The detector size is half of the width and radius, respectively, and is given in AUs. The lines show the calculations according to Eq. (18) with the parameters from Eq. (19).

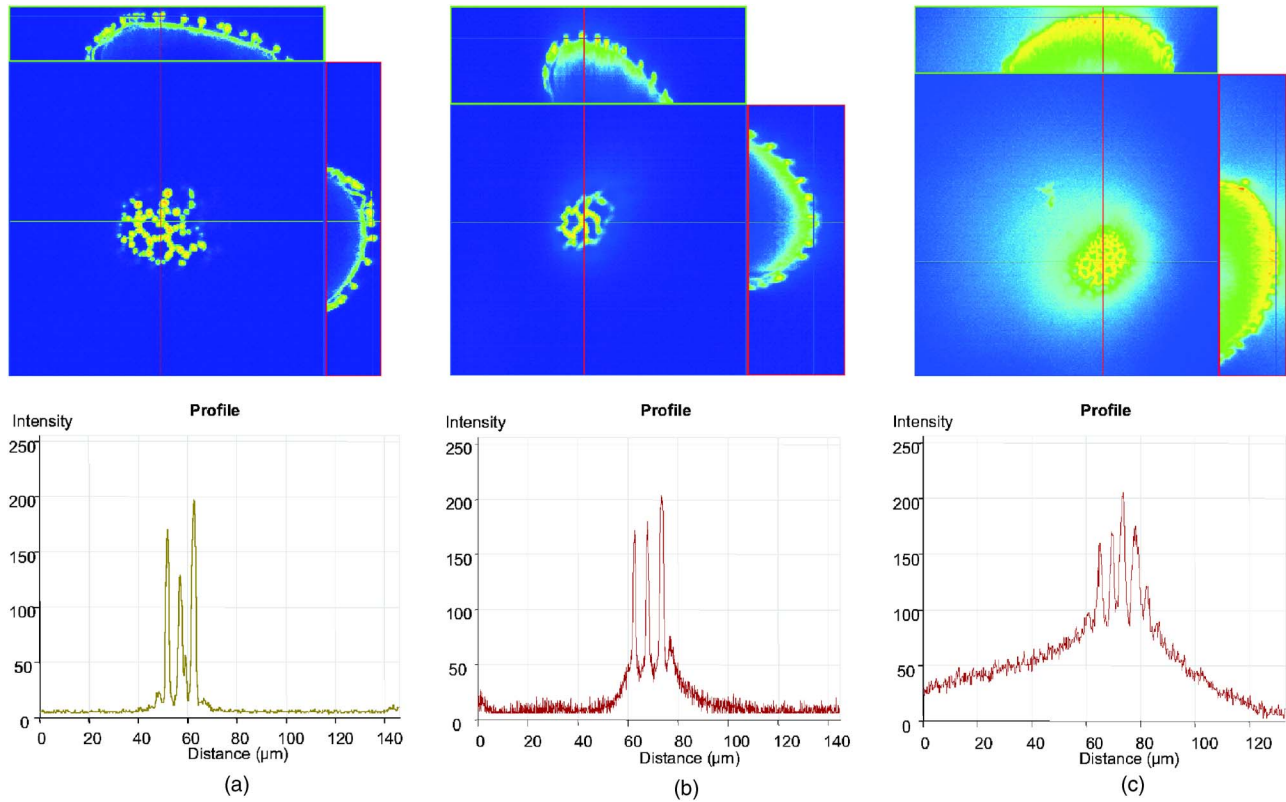


Fig. 16 Imaging of pollen grains using (a) point scanning LSM 510 META, (b) L2M (LSM 5 LIVE), and (c) MSM (Ultraview LCI, Yokogawa CSU 21). All images were taken using a Zeiss Plan-Apochromat 63×/1.4 oil lens (excitation: 488 nm, fluorescence: >505 nm). The upper row shows a single optical slice and cut sections along the lines in the image. The lower row depicts line scans through the images above. For (a) and (b), the pinhole was set to 1 AU.

transmission efficiency of the Achrogate used is.

$$T = \frac{A_{Pupille} - A_{RL}}{A_{Pupille}} = \frac{\pi r^2 - 2br}{\pi r^2} = 1 - \frac{2b}{\pi r}, \quad (25)$$

where r is the pupil radius (2.5 mm), and b is the line width of the reflective area. Only the fluorescence light that impinged onto the central reflective area is lost. The excitation light is focused down to the 100- μm -wide line. Thus, nearly 98% of the illumination light is delivered to the sample by the Achrogate, independently of the wavelength. Likewise, 98% of the fluorescence light is transmitted under these circumstances. This is independent of the wavelength too, which is especially beneficial when multiple excitation lines are simultaneously used or if fast multitracking is used. However it has to be noted that the spatial incoherence of the fluorescence yields the discrimination of excitation and detection as explained above. This means that reflection imaging cannot be performed with the Achrogate.

3.2 Characterization of the Microscope

To characterize the optical resolution of the microscope system, the PSF and the depth discrimination were measured. The latter is important when imaging thick samples, because it characterizes the ability of the microscope to suppress out-of-focus signals. The results were compared to a point scanning confocal microscope Zeiss LSM 510 META and to a MSM. For the MSM we chose a spinning disk system Ultra-

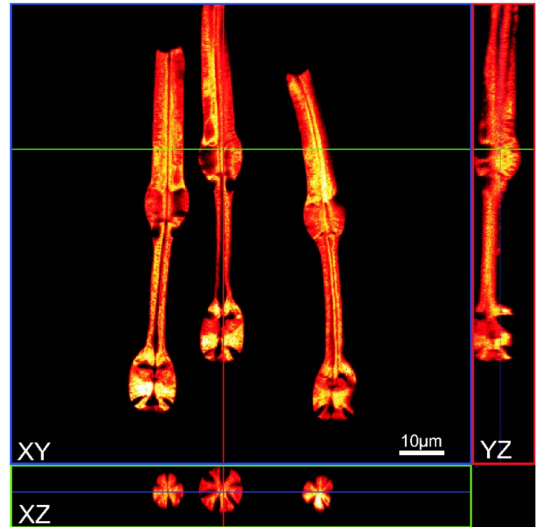


Fig. 17 Structural organization of pharynx muscles in live *Caenorhabditis elegans*: series of z stacks through the anterior body parts nematode larvae were imaged with a Zeiss Plan-Apochromat 63×/1.4 oil objective lens with 488-nm excitation, at an effective pixel size of 200 nm (512×512 pixels) and z spacing of individual sections of 200 nm. Speed of image acquisition: 120 frames per second. The figure shows an individual optical section out of an xyz series (xy) as well as two selected orthogonal cuts (xz and yz). Complete z stacks of 69 images were acquired within 602 ms using a piezofocus in bidirectional z-scanning mode.

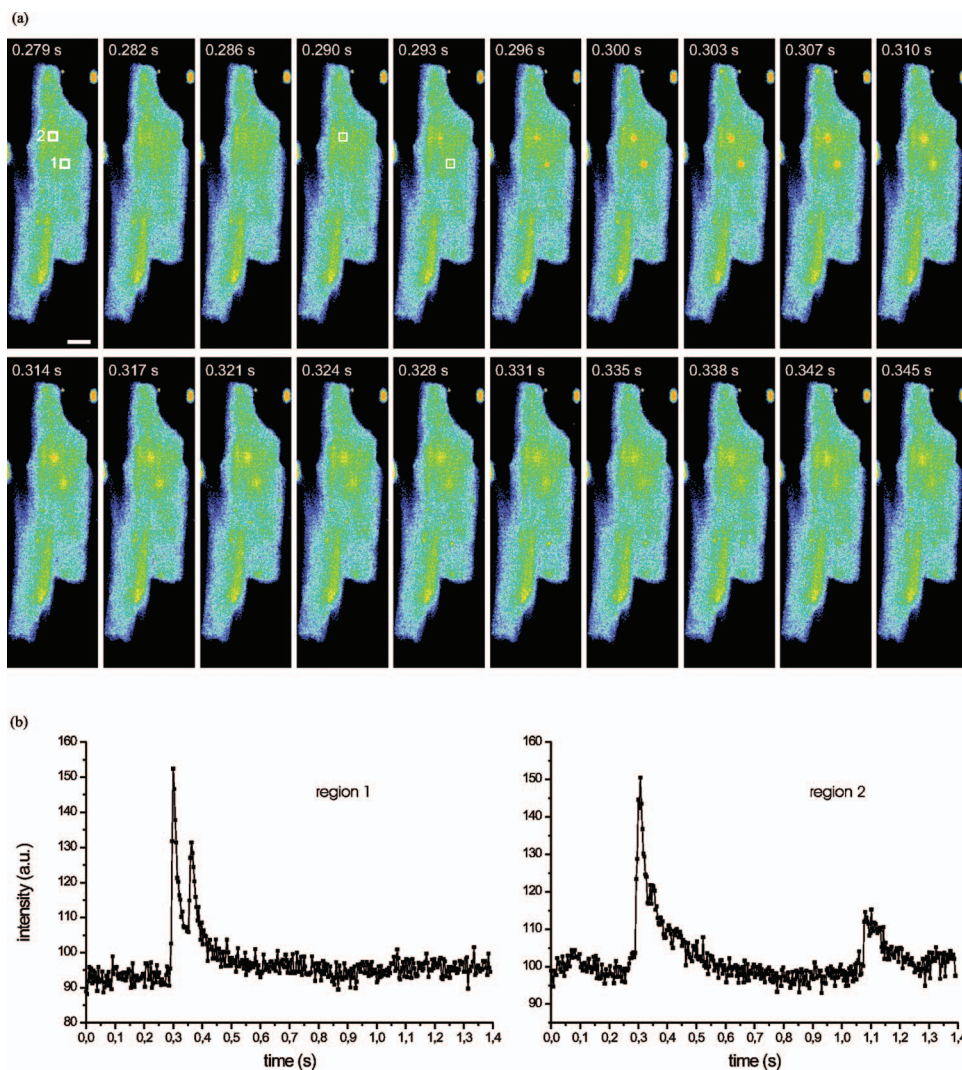


Fig. 18 Calcium sparks in isolated live cardiac muscle cell imaged with a Zeiss Plan-Apochromat $63\times/1.4$ oil objective lens. Pixel size: $0.39\times 0.39\ \mu\text{m}^2$, image acquisition rate: 288 frames per second. (a) Subset of consecutive images depicting localized calcium release events at two isolated sites (ROIs 1 and 2). Scale bar $10\ \mu\text{m}$. (b) Intensity traces of fluorescence signal recorded from ROIs 1 and 2 as shown in (a).

view LCI, Yokogawa CSU 21 (Perkin Elmer, USA). The LSM 510 META and the MSM were both mounted on a Zeiss Axiovert 200 M.

The PSF was measured using fluorescing beads (diameter $110\ \text{nm}$, excitation $488\ \text{nm}$, emission $>505\ \text{nm}$, Molecular Probes, USA) and a Zeiss Plan-Apochromat $63\times/1.4$ objective lens. Typical plots of the lateral and axial PSF for both systems are shown in Fig. 12. The unsymmetrical shape of the PSF of the LSM is due to the vectorial nature of the light fields (i.e., polarization effects) that have not been considered in Sec. 2. The asymmetry of the PSF of high-NA objectives in a LSM with linear polarized illumination can be comparable to the asymmetry observed in the L2M due to the line illumination and detection. Given the right orientation of the polarization in a L2M (perpendicular to the line illumination) both effects can partially compensate each other as can be seen in Fig. 12. Table 1 gives a comparison of the measured values in the confocal limit with theoretical calculations taking the vectorial nature of the light into account.⁹ Because the bead's size is not negligible with respect to the lateral size of the PSF of

the oil immersion objective, the values given as measured in Table 1 have been obtained after deconvolution of the measured PSF with the spherical beads.

The FWHM for the lateral and the axial resolution shown in Fig. 13 was similar on both systems or even somewhat smaller for the L2M as expected (see Fig. 4 and theoretical curves) and in agreement with data that have been reported elsewhere.³ Here we give average values of the lateral widths measured and theoretical curves based on the scalar theory presented before. The agreement with the theory is quite reasonable in the lateral direction (see also Table 1). In the axial direction, the discrepancies to the theory are probably due to any residual aberrations present.

The depth discrimination was acquired by measuring z stacks close to the interface of a homogeneously stained slide [Delta Vision fluorescence slide (green), USA]. To match the deconvolution of the objective lens, a standard cover slip was mounted on the interface using immersion oil. The average signal per frame versus the axial position relative to the interface was calculated. To this end, background signals

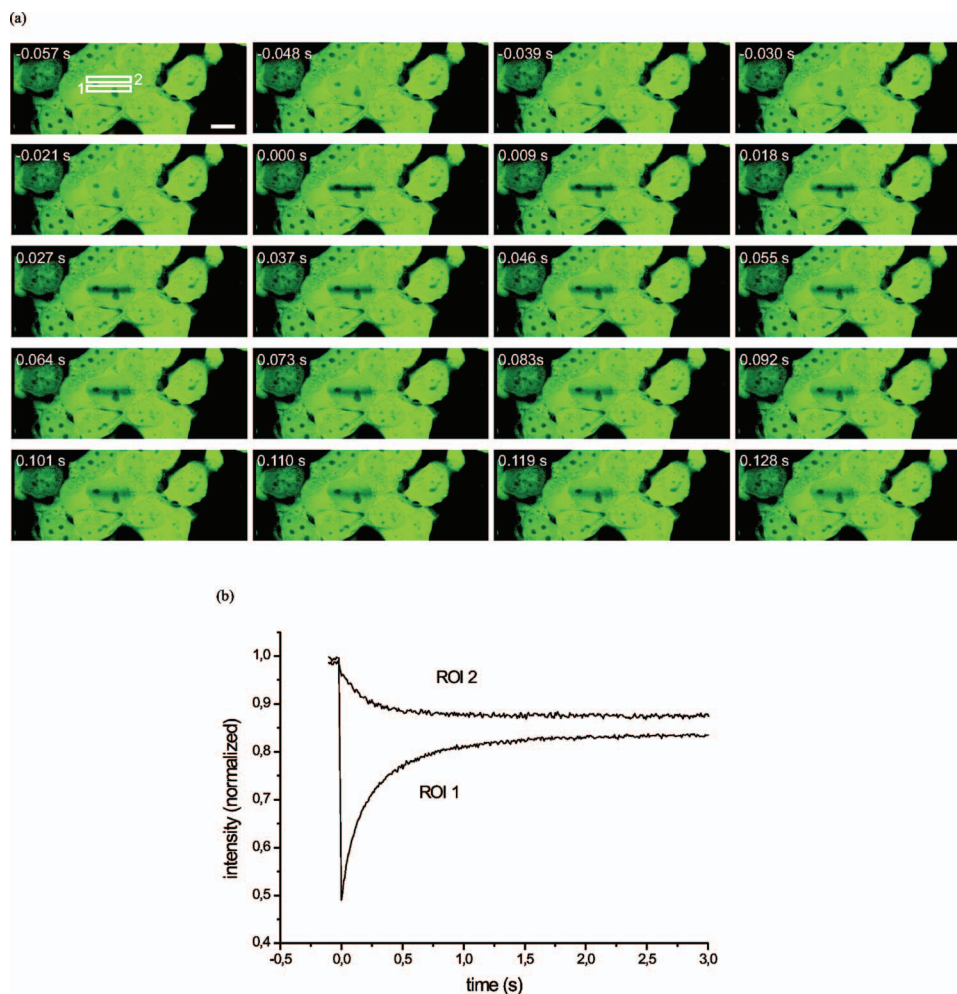


Fig. 19 FRAP in HEp-2 cells imaged with a Zeiss Plan-Apochromat $63\times/1.4$ oil objective lens at 488-nm excitation. Pixel size: $0.2\times 0.2\ \mu\text{m}^2$, image acquisition rate: 108 frames per second. The image acquisition at $t=0\ \text{s}-0.0021\ \text{s}$ was followed by localized photobleaching within ROI 1 (bleach time 12 ms). (a) Image sequence, (b) temporal analysis of redistribution of nonbleached EGFP within ROI 1 and adjacent ROI 2.

obtained with the laser turned off were subtracted from the data and the data were normalized by the maximum signal measured inside the slide. Typical curves measured with a Zeiss Plan Apochromat $63\times/1.4$ oil objective lens are plotted in Fig. 14 for the LSM 5 LIVE, the LSM 510 META, and a MSM Ultraview LCI. The pinhole diameter for the LSM 5 LIVE and LSM 510 META were set to 1 AU. The pinhole diameter on the Ultraview is fixed and is not known to us. For reference, the trace for the LSM 510 META with the pinhole set to 10 AU is also shown. The measured curves are in reasonable agreement with the theoretical curves obtained using the scalar theory.

Slit detection results in a reduced depth discrimination of the LSM 5 LIVE as compared to the point scanning confocal detection as shown and discussed in Sec. 2. The slope of the trace at the edge is similar to the slope of the LSM 510 META at a pinhole size of 1 AU demonstrating the similar axial resolution of both systems. However, the MSM Ultraview LCI showed almost no depth discrimination, which demonstrates that it is strongly limited by the above-mentioned constant background signal in the depth response. Very similar results have been obtained by Reichelt and Amos.¹⁰

A more direct way to determine the depth discrimination is to use a thin fluorescing sheet and to record the signal intensity as a function of focus position. The following measurements were made using such a 100-nm thick object obtained from the University of Amsterdam, the Netherlands.¹¹ The FWHM of the depth discrimination as a function of slit- and pinhole-size, respectively, was determined for an objective lens Plan-Neofluar $20\times/0.5$ (Fig. 15). The experimental data agree well with the theoretical predictions from Sec. 2. A detailed comparison of different microscope types with respect to signal-to-background ratio for thickly stained samples is given in Ref. 12.

The difference of the L2M and the LSM with regard to depth discrimination becomes more evident when looking at the depth responses themselves exhibiting a weaker falloff of the signal with defocus. Despite these differences to a point scanning microscope, the system provides sufficient sectioning and depth discrimination even for thick samples as we will show below. Figure 16 shows a single optical slice and cut sections through autofluorescent pollen grains (from Karolinsky Institute, Stockholm, Sweden) for a point scanning

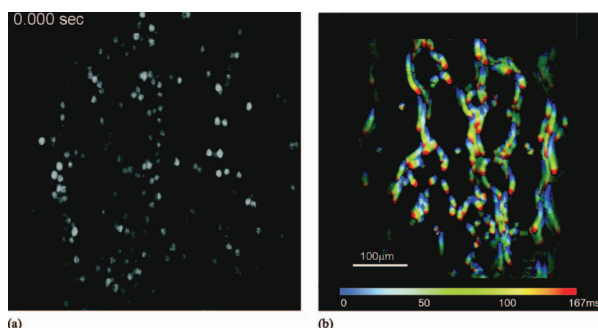


Fig. 20 Blood flow in a mouse embryo (yolk sac region, 8.5 days postfertilization, shown are primitive erythroblasts ϵ -globin expressing GFP) imaged with a Zeiss Plan-Neofluar $20\times/0.75$ objective lens at 180 frames per second (256×256 pixel) using the L2M (LSM 5 LIVE). Field of view: $500\times 500\ \mu\text{m}^2$. (a) Image at a single time point; (b) color encoded time projection of 30 frames showing trajectories of blood flow.

confocal microscope, the L2M, and a MSM all imaged with a Zeiss Plan-Apochromat $63\times/1.4$ oil objective lens. We carefully selected pollen grains with the same structure and similar diameters (about $50\ \mu\text{m}$) for the measurements at each microscope. Detector gain and offset were adjusted such that the full dynamic range of each detector was used. Line plots have been extracted from the optical slice and are shown below each image. It can be seen that the point scanning microscope has the best optical sectioning capabilities followed by the L2M. However, the depth discrimination of the MSM is strongly reduced by out-of-focus light. This can be seen by the high degree of blur that is present around the in-focus information (bright structures). This is also partly due to the suboptimal pinhole diameter for the magnification of the lens used.

4 Applications Using the L2M

As has been shown above, the L2M it is well suited for imaging fast processes in cells and tissue with 3D resolution. In combination with a fast and sensitive line camera with a line rate of 60 kHz processes occurring on a millisecond and even microsecond timescale can be observed in live specimen. These processes include active transport phenomena, signaling, and molecular interactions at membranes as shown in Fig. 1.

As one example, we show results of studying structural features of live motile nematodes. To avoid artifacts induced by movement of the animals, z series of confocal sections through anterior body parts of green fluorescent protein (GFP)-expressing *Caenorhabditis elegans* (GFP expression in pharynx muscles) were taken at an acquisition rate of 120 frames per second (512×512 pixels) and a confocal slit size corresponding to 1 AU (samples provided by Prof. Ralf Baumeister and Dr. Roland Nitschke, Freiburg University, Germany). By focusing through the specimen with a piezodriven objective focusing device complete z stacks consisting of 69 optical sections spaced at 200-nm intervals could be captured every 602 ms. The piezodriven objective focus was operated in bidirectional mode so that the time interval between adjacent z stacks was minimized. In addition to dem-

onstrating the speed performance of the L2M, Fig. 17 also illustrates the optical sectioning capabilities of the system.

In a second example, isolated live rat cardiomyocytes loaded with the calcium indicator dye Fluo-4 were imaged in xyt imaging mode at 288 frames per second with 512×200 pixels (samples prepared by Dr. W. J. Lederer and L.-S. Song, Medical Biotechnology Center, University of Maryland Biotechnology Institute, Baltimore, Maryland). Figure 18(a) shows a subset of consecutive images taken out of a 8000-image time series acquired with the L2M. The series depicts localized events of transient calcium release (calcium sparks within regions of interest 1 and 2; see also Ref. 13). Closer analysis of the temporal evolution of the calcium dynamics at individual release sites reveals that an acquisition speed well beyond 100 frames per second is indeed necessary to capture the overall events (with typical halftimes of 25 to 50 ms) and, in particular, the rapid upstroke of the fluorescence signal triggered by the opening of calcium release channels at the muscle cell's sarcoplasmic reticulum [Fig. 18(b)].

In a third example, we combined the L2M with a point scanner-based laser photomanipulation system (Carl Zeiss LSM DuoScan) to study in a fluorescence recovery after photobleaching (FRAP) approach the mobility of free enhanced GFP (EGFP) in HEp-2 cell cultures (Fig. 19). These experiments were performed at an acquisition rate of 108 frames per second (512×100 pixels) and with a confocal slit size corresponding to 1 AU. The image acquisition was interleaved with a localized photobleaching event employing a 488-nm laser light and lasting for 12 ms [bleaching within region of interest 1 depicted in Fig. 19(a)]. The temporal analysis of redistribution of nonbleached EGFP within region of interest (ROI) 1 and an adjacent ROI 2 of these experiments shows that the imaging speeds that we attained with the L2M are well suited and indeed required to characterize the mobility of the fluorescent protein within the cell nucleus (half-time of recovery approximately 200 ms) [Fig. 19(b)]. Finally, we show the dynamics of blood flow observed in mouse embryos that were 8.5 days postfertilization (samples prepared by Prof. Scott Fraser, Dr. Mary Dickinson, and Elizabeth Jones, Imaging Center, Caltech, Pasadena, California). At this stage, the size of the embryo was about 4 mm. GFP-expressing blood cells were imaged inside the yolk sac at a depth of about $400\ \mu\text{m}$ using 488-nm excitation light, again at a confocal slit size corresponding to 1 AU. Due to the good optical sectioning capabilities and the high temporal resolution of the microscope, we were able to acquire snapshots of the blood flow at different optical sections and time points. Figure 20 (left side) shows a single snapshot of individual blood cells taken at a speed of 180 frames per second. The blood cells appear round shaped and free from smearing effects caused by inappropriate acquisition times. The right panel of Fig. 20 shows a color projection of 30 frames at adjacent time points with the color gradient illustrating the positions of the individual blood cells at different time points. It was possible to continuously track the blood cells with velocities greater than 10 mm/s (see also Refs. 14 and 15). The feature size that needed to be resolved is quite big (about $10\ \mu\text{m}$) in comparison to the optical resolution. One benefit of the used instrument is that the sampling can be adapted at

least in one image axis to the feature size of the investigated specimen in order to reduce data, to improve sensitivity, and/or to increase frame speed.

5 Discussion and Conclusions

We have shown both theoretically and experimentally that the CLSM has superior depth discrimination if compared to parallel scanning confocal microscope systems. Hence, CLSMs are well suited for investigations in three dimensions at the microscopic scales, especially in thick samples. They can also be best adapted to scanning particular ROIs, due to their flexibility in their scanning regime. However, the temporal resolution of such systems remains clearly behind the speed of most biological processes on the cellular level. Due to the limited amount of fluorescence that can be extracted from a diffraction limited point within a biological sample, there are fundamental limits to the increase of speed of point scanning microscopes.

A simple estimate can give a feeling for the limitation set by the detection of fluorescence photons. If one assumes a fluorochrome concentration of 10^{-6} mol/l within a resolution volume (voxel) of $1 \mu\text{m}^3$, the maximum emission rate is 10^{12} photons/s for a fluorochrome with a lifetime of 1 ns. Due to the finite collection and detection efficiency about 10^{10} electrons/s can be generated by this photon flux in a detector. This means we have to integrate over at least 10 ns to achieve a shot-noise limited signal-to-noise ratio of 10 ($10^2/10^{10} \text{ s}^{-1} = 10^{-8} \text{ s}$). Therefore, with $512 \times 512 \times 50$ pixels and a point-by-point imaging approach, the fastest 3D image acquisition rate possible is about 10 per second. This means that from a fundamental point of view and making favorable assumptions (e.g., maximum emission rate without bleaching) only relatively slow imaging can be achieved in a point scanning approach to 3D imaging.

In order to achieve imaging in the millisecond range, a parallel acquisition of several hundred voxels is required. MSMs, mainly spinning disk systems, are widespread for this application. The depth discrimination is comparable to the LSM for thin samples. However, it is compromised by the cross talk between adjacent illumination and detection spots present when imaging thick samples. This means that they are not well suited for imaging samples, which are much thicker than a few cell layers. Moreover spinning disk systems use fixed confocal apertures. The optical sectioning cannot be adjusted for different objective lenses or if the signal to noise of the detected signal is too low. The scanning principle in a spinning disk system relies on a matrix detector, whereas at each position of the disk only part of the sensor is configured to receive signals from the sample. In the remaining pixels, dark noise is accumulated, which decreases the overall sensitivity of the system.

Line illumination and detection allows one to circumvent many of the problems of the spinning disk systems. The L2M represents a novel approach for fast fluorescence imaging of dynamic processes in biomedical applications. The highly parallel illumination and detection scheme results in acquisition speeds using up to two confocal channels of greater than 100 full frames per second at 512×512 pixels. Reducing the frame size, even faster dynamic processes can be investi-

gated. Due to the use of innovative concepts for wavelength-independent beamsplitting and efficient generation of a homogeneous illumination pattern, it allows for at least 10 times faster imaging of typical biological samples as compared to the state of the art point scanning microscope systems. The optical resolution is comparable to confocal point scanning systems, and the adjustable confocal aperture allows one to vary the optical slice thickness. Its depth discrimination is superior to multispot-type scanning microscopes. We have demonstrated the flexibility of the L2M to image at different optical resolutions, different frame geometries, and different acquisition rates and to trade those parameters for sensitivity.

Acknowledgments

We thank Prof. Scott Fraser, Dr. Mary Dickinson, and Elizabeth Jones from the Biological Imaging Center, Caltech; Dr. W. J. Lederer and L.-S. Song, Medical Biotechnology Center, University of Maryland Biotechnology Institute, and Prof. Ralf Baumeister and Dr. Roland Nitschke, Freiburg University (Freiburg, Germany) for providing the samples and supporting the application test.

References

1. J. P. Pawley, "Light paths of current commercial confocal light microscopes for biology," in *Handbook of Biological Confocal Microscopy*, J. B. Pawley, Ed., pp. 2, 581–598, Plenum Press, New York (1995).
2. G. J. Brakenhoff and K. Visscher, "Confocal imaging with bilateral scanning and array detectors," *J. Microsc.* **165**, 139 (1993).
3. T. Corle and G. Kino, "Slit microscopes," in *Confocal Scanning Optical Microscopy and Related Systems*, chap. 2, pp. 97–103, Academic Press, San Diego (1996).
4. S. Kawata, R. Arimoto, and O. Nakamura, "Three-dimensional optical-transfer-function analysis for a laser-scan fluorescence microscope with an extended detector," *J. Opt. Soc. Am. A* **8**, 171 (1991).
5. W. B. Amos and J. G. White, "Direct view confocal imaging systems using a slit aperture," in *Handbook of Biological Confocal Microscopy*, J. B. Pawley, Ed., chap. 25, pp. 403–415, Plenum Press, New York (1995).
6. J. B. Guild and W. W. Webb, "Line scanning microscopy with two-photon fluorescence excitation," *Biophys. J.* **68**, 290 (1995).
7. S. W. Hell and E. H. K. Stelzer, "Lens aberrations in confocal fluorescence microscopy," in *Handbook of Biological Confocal Microscopy*, J. P. Pawley, chap. 20 pp. 347–354, Plenum Press, New York (1995).
8. V. Andresen, A. Egner, and S. W. Hell, "Time-multiplexed multifocal multiphoton microscopy," *Opt. Lett.* **26**, 75 (2001).
9. C. J. R. Sheppard and H. J. Matthews, "Imaging in high-aperture optical systems," *J. Opt. Soc. Am. A* **4**, 1354 (1987).
10. S. Reichelt and W. B. Amos, "SELS: A new method for laser scanning microscopy of live cells," *Imaging and Microscopy* **11**, 9 (2001).
11. G. J. Brakenhoff, G. W. H. Wurpel, K. Jalink, L. Oomen, L. Brocks, and J. M. Zwier, "Characterization of sectioning fluorescence microscopy with thin uniform fluorescent layers: Sectioned imaging property or SIPcharts," *J. Microsc.* **219**, 122 (2005).
12. D. R. Sandison and W. W. Webb, "Background rejection and signal-to-noise optimization in confocal and alternative fluorescence microscope," *Appl. Opt.* **33**, 603–615 (1994).
13. L.-S. Song, S. Guatimosim, L. Gómez-Viquez, E. A. Sobie, A. Ziman, H. Hartmann, and W. J. Lederer, "Calcium biology of the transverse tubules in heart," *Ann. N.Y. Acad. Sci.* **1047**, 99 (2005).
14. M. Liebling, A. S. Farouhar, M. Gharib, S. E. Fraser, and M. E. Dickinson, "4-dimensional cardiac imaging of living embryos via post-acquisition synchronization of nongated slice-sequences," *J. Biomed. Opt.* **10**, 054001 (2005).
15. A. S. Farouhar, A. S. Hickerson, M. Liebling, A. Moghaddam, J. Lu, H.-J. Tsai, J. R. Hove, S. E. Fraser, M. E. Dickinson, and M. Gharib, "The embryonic zebrafish heart as a resonance suction pump," *Science* **312**, 751–753 (2006).